PHYSICAL REVIEW B VOLUME 3, NUMBER 10 15 MAY 1971

Quantum Field Theory of Inelastic Diffraction. II. Two-Step Inelastic Diffraction*

G. E. Laramore† and C. B. Duke
Department of Physics, Materials Research Laboratory and Coordinated Science Laboratory, University of Illinois, Urbana, Illinois 61801
(Received 7 December 1970)

The consequences of a two-step model of inelastic diffraction are investigated with emphasis on displaying the importance of the relevant conservation laws of total energy and of the component of momentum parallel to the surface. The inelastic energy, loss, and angular profiles for electrons scattered from W(100) are calculated using a model embodying primary Bragg elastic scattering and schematic forms for the coupling between the beam electrons and the elementary excitations of the solid. In general, two peaks in the inelastic energy profile are associated with each peak in the elastic energy profile. Conservation of the component of momentum perpendicular to the surface for the case of a bulk excitation gives rise to a new phenomenon: sideband diffraction. This effect is quite apparent in the angular profiles. Semiquantitative calculations are performed for inelastic diffractions from Al(100) associated with bulk- and surface-plasmon losses. In these calculations we use the sharp-junction semi-infinite jellium model to describe the plasmon dispersion curve, the plasmon lifetime, and the plasmon coupling to the beam electrons.

I. INTRODUCTION

In any consideration of inelastic electron diffraction, the target solid must be treated as a dynamical system in order to allow for energy transfer between the beam electrons and the solid. Therefore in an earlier paper[1] (hereafter referred to as I) we developed a quantum field perturbation theory to describe the creation of boson excitations in the solid with the simultaneous loss of energy by the incident electron. In this paper we present a detailed discussion of the dominant inelastic-diffraction phenomena predicted by this theory. Preliminary descriptions of some of the predicted phenomena have appeared elsewhere.[2-4]

The objective of the analysis presented in this paper is the use of the increasingly satisfactory model descriptions[4-6] of elastic low-energy-electron diffraction (LEED) plus simple models of the electronic-loss processes to predict the inelastic cross sections in terms of independently determined parameters characterizing the electron-solid system. In our view, there are two major motivations for this analysis. First, as discussed in I, we expect that microscopic calculations of elastic LEED intensity profiles are likely to be less satisfactory than semiempirical descriptions of these profiles for some years. Therefore we require a model of inelastic LEED into which semiempirical parametrizations of elastic LEED intensities can be inserted. The model developed in I exhibits this attribute, which we utilize herein to predict the plasmon-emission cross sections from Al(100) in terms of the known elastic LEED intensity profiles.[4] Second, if the accuracy of the qualitative features of the model predictions is vindicated, then the analysis can be used to identify the nature of the electronic energy-loss mechanisms in cases where these mechanisms are unknown or ambiguous.[3] For this purpose, a critical feature of the model predictions is their sensitivity to the details of the parameters characterizing the elementary excitation spectrum of the target and the interaction of these excitations (referred to as "loss modes") with the incident electrons. We devote considerable attention herein to the examination of this issue.

Our analytical procedure is a six-step process. First, we parametrize the elastic electron-lattice interactions by analyzing elastic LEED intensities. Second, we study the effect of changing the beam parameters (incident electron energy E and angles of incidence θ, ψ) on a prominent feature of the elastic intensity profile which will influence the inelastic cross sections (for example, the structure at "high" energies near the energy of a kinematical Bragg resonance). Third, using a particular model we calculate the inelastic cross sections for beam parameters in the neighborhood of this structure. Fourth, we examine in detail the variation with beam parameters of the inelastic cross sections as a functional of the nature of the electron-loss-mode coupling, the loss-mode dispersion relation, and the perturbation-theory approximation used in the calculation. Fifth, we test the model in a simple case for which most of the coupling mechanisms and parameters are thought to be known. Finally, if the test indicates the adequacy of the model, it will be applied to analyze data in more complicated cases. In this paper we carry out the procedure through a first attempt at step five. The completion of step five and, hopefully, passage to step six

await the availability of more extensive experimental data.

The considerations given in I permit us to restrict our numerical calculations in several respects. First, they indicate that published experimental data [7–12] demonstrates the predominance of a two-step inelastic diffraction mechanism. [1–4] Therefore we consider here only this contribution to the inelastic cross section. Second, we set up in I and use herein a series of five models describing various possible aspects of electron-plasmon interactions. Within these restrictions we examine the qualitative features of the model predictions for the (100) face of a bcc metal with the lattice parameters of tungsten. We select as our presumably "simple" test case plasmon emission for Al(100). The motivations for this selection are that elastic LEED is described well by our model[4] and the electron-plasmon vertices are thought to be described by simple models with known parameters. [1–4] In this case we also consider the effects of a number of refinements (e.g., plasmon damping and multiple scattering in the elastic electron-lattice vertex).

Having noted the extent of our analysis, it seems appropriate to conclude this Introduction with an indication of its main predictions. As the inelastic cross sections depend on six variables, a necessary preliminary to this indication is an explanation of our methods of presenting the results of our calculations. The state of the incident electrons can be specified by the incident beam energy E and the incident beam direction (θ, ψ), where the polar axis is taken perpendicular to the solid surface, and the azimuthal angle ψ is measured relative to an axis in the crystal face. Similar considerations hold for the scattered electrons with energy E' and direction given by (θ', ψ'). However, instead of E' it is generally more convenient to use w, the energy lost by the electrons, as a variable

$$w = E - E' . \tag{1.1}$$

In presenting the results of our calculations we have chosen to allow only one of the above parameters to vary at a time. Also we restrict ourselves exclusively to the case of scattering in a plane (i.e., $\psi = \psi'$). In each instance our calculational results are given as a diffracted intensity profile as a function of a given variable. This generates what we shall term an "energy profile," a "loss profile," or an "angular profile" depending on the relevant variable. These are defined more precisely as follows. (a) In the case of an *energy profile* we hold fixed the direction (θ, ψ) of the incident beam, the direction of the scattered beam (θ', ψ'), and the loss energy w. We calculate the scattered intensity as a function of incident beam energy E. (b) In the case of a *loss profile* we hold fixed the direction (θ, ψ) and the energy E of the incident beam and the direction (θ', ψ') of the scattered beam. We calculate the scattered intensity as a function of the loss energy w. (c) In the case of an *angular profile*, we hold fixed the direction (θ, ψ) and energy E of the incident beam as well as the loss energy w. We calculate the scattered intensity as a function of the final angle θ' (with $\psi' = \psi$).

We recall from I that for two-step inelastic diffraction, two types of resonant phenomena are evident in the inelastic cross sections. [1,2] Individual resonances in the elastic LEED intensity profile lead to double "energy-tuned" resonances in the inelastic energy profile. The vestiges of momentum conservation normal to the surface of the solid lead to momentum-tuned resonances for any mechanism of inelastic diffraction via the excitation of bulk loss modes. Consider, for example, the case of the inelastic energy profiles. If a resonance occurs at an incident beam energy of E_B in the elastic channel, in the inelastic channel we observe a resonance at energy E_B for the case of lattice scattering before energy loss[7] and a resonance at $(E_B + w)$ for the case of energy loss before scattering from the lattice. [8,9] The momentum-tuned resonances can cause an enhancement of portions of these peaks and, more spectacularly, can cause the two peaks to become four peaks. [2–4] However, this effect is not very pronounced for plasmon excitations which have rather flat dispersion relations. [13] This is especially true when plasmon lifetime effects are taken into account. [14–16] Nevertheless, the momentum-tuned resonances produce a large effect in the angular profiles even when plasmon lifetime effects are taken into account. They give rise to a characteristic doublet structure when the incident beam energy is near an energy resonance value. Thus, for bulk-plasmon emission we see a characteristic change in the angular profile from a singlet to a doublet and then back to a singlet as the energy is "swept" over a resonance value. In the case of surface-plasmon emission the angular profiles *always* have a doublet structure.

In Sec. II we state for reference the relevant expressions for the inelastic-scattering cross section which were derived in Paper I. In Sec. III we present and discuss schematic calculations of the various intensity profiles for the case of energy loss due to creation of a "bulk" excitation. Target parameters corresponding to W(100) are used in our model calculations. In Sec. IV we discuss the relevant features of the profiles when a "surface" excitation is created. Then we present in Sec. V a detailed calculation of the inelastic diffraction from Al(100) for the case of bulk- and surface-plasmon emission. In these calculations we use the electron-plasmon interaction vertices charac-

teristic of semi-infinite jellium.[17] Finally, in Sec. VI we summarize our results.

II. INELASTIC-SCATTERING CROSS SECTION IN THE TWO-STEP DIFFRACTION APPROXIMATION

In this section we specify the expression for the inelastic-scattering cross section in the two-step diffraction approximation. The reader is referred to I for a derivation. The cross section can be written as

$$\frac{d^2\sigma}{dEd\Omega} = \left(\frac{E-w}{E}\right)^{1/2}(2\pi)^{-3}\sum_{\vec{g}}\sum_{\vec{p}}\frac{(2\pi)^2}{A}\,\delta(\vec{k}_{\parallel'}+\vec{p}_{\parallel}-\vec{k}_{\parallel}-\vec{g}) \times[-2iN(-w)\mathrm{Im}D(\vec{p},w)] \times M(k_\perp(0,E),k_\perp'(0,E-w),p_\perp,\vec{g}) \times|A_b(\vec{g},p_\perp,E,w)+A_c(\vec{g},p_\perp,E,w)|^2 . \quad (2.1)$$

In Eq. (2.1) E denotes the energy of the incident beam, w the loss energy, $\vec{k}$ the wave vector of the incident electron, $\vec{k}'$ the wave vector of the scattered electron, $\vec{p}$ the wave vector of the excitation created in the solid, and $\vec{g}$ a two-dimensional reciprocal-lattice vector resulting from the translational periodicity of unit cells of area A parallel to the surface. The subscripts $\parallel$ and $\perp$ are defined relative to the surface of the solid. The quantities $N(w)$ and A_i are given by

$$N(w) = (e^{w/\kappa T}-1)^{-1} , \quad (2.2)$$

$$A_b(\vec{g},p_\perp,E,w) = \frac{t(E)}{\{1-R[k_\perp(0,E),k_\perp(\vec{g},E),0;\vec{g}]\}k_\perp(\vec{g},E)}\left(\frac{R[k_\perp'(0,E-w),-k_\perp(\vec{g},E),-p_\perp;0]-1}{i[k_\perp'(0,E-w)-k_\perp(\vec{g},E)-p_\perp]d}\right) , \quad (2.3)$$

$$A_c(\vec{g},p_\perp,E,w) = \frac{t(E-w)}{\{1-R[k_\perp'(0,E-w),k_\perp'(-\vec{g},E-w),0;\vec{g}]\}k_\perp'(-\vec{g},E-w)}\left(\frac{R[k_\perp(0,E),-k_\perp'(-\vec{g},E-w),-p_\perp;0]-1}{i[k_\perp(0,E)-k_\perp'(-\vec{g},E-w)-p_\perp]d}\right) , \quad (2.4)$$

$$R[k_{\perp 1},k_{\perp 2},p_\perp;\vec{g}] = \exp\{i[k_{\perp 1}+k_{\perp 2}+p_\perp]d-i\vec{g}\cdot\vec{a}\} . \quad (2.5)$$

In Eqs. (2.3)–(2.5), $k_\perp(\vec{g},E)$ is the solution of

$$G^{-1}(\vec{k}+\vec{g},E) = E-\frac{\hbar^2}{2m}(\vec{k}_{\parallel}+\vec{g})^2-\frac{\hbar^2k_\perp^2(\vec{g},E)}{2m} - \Sigma(\vec{k}+\vec{g},E) = 0 . \quad (2.6)$$

The quantity $\vec{a}$ is a vector which defines the relative shift between adjacent layers of the solid, d designates the distance between adjacent layers,[18] and $D(\vec{p},w)$ is a renormalized loss-mode propagator having the general form

$$D(\vec{p},w) = [w-\hbar w(\vec{p})+i\Gamma(\vec{p})]^{-1} - [w+\hbar\omega(\vec{p})+i\Gamma(\vec{p})]^{-1} , \quad (2.7)$$

where $\hbar\omega(\vec{p})$ is the loss-mode dispersion relation and $\hbar/\Gamma(\vec{p})$ is the lifetime of the mode.[19] The factors of $\{[R(x)-1]/x\}$ in Eqs. (2.3) and (2.4) are the "central-cell" corrections described in Appendix A of I. They are caused by the fact that in the jellium model, the plasmon fields are continuous whereas the elastic electron-lattice interaction is cell periodic. As we anticipate that the plasmon field also is cell periodic in an actual solid, we set $[(R(x)-1)/x]\equiv 1$ in Refs. 2–4. Although these factors make little difference in the shape of the cross sections predicted by the numerical calculations, we retain them for completeness in our model problem. Unfortunately, their dependence on $p_\perp$ complicates the algebra relative to Refs. 1–4. The main consequence of this fact is the failure of our definition of M in Eq. (2.1) to coincide with the definition of the analogous M_i quantities in Sec. IV B of I because the factor of $|A_b+A_c|^2$ is not independent of $p_\perp$ unless we take the continuum limit [I, Appendix A].

For the purpose of our numerical work we adopt the s-wave model to describe scattering of an electron from an ion core of the solid[1,18]

$$t(E) = h^2(e^{2i\delta(E)}-1)/4\pi ikm . \quad (2.8)$$

We also use a particularly simple model[18] for the electronic self-energy $\Sigma(\vec{k},E)$ which appears in Eq. (2.6), i.e.,

$$\Sigma(\vec{k},E) = -V_0-i\Gamma(E) , \quad (2.9)$$

where

$$V_0 = \zeta+\phi \quad (2.10a)$$

and

$$\Gamma(E) = (\hbar^2/m\lambda_{ee})[(2m/\hbar^2)(E+V_0)]^{1/2} . \quad (2.10b)$$

In Eqs. (2.10) ζ is the Fermi energy, ϕ is the work function, and λ_{ee} is twice the mean free path of the electron in the material.

Finally, $M(k_\perp(0,E-w),k_\perp'(0,E-w),p_\perp,\vec{g})$ is a quantity whose form depends both on the kind of excitation involved and on the nature of the electronic interactions with the excitation. For "bulk" excitations, it contains the sideband-diffraction resonances. In Secs. III A–III C we discuss the results

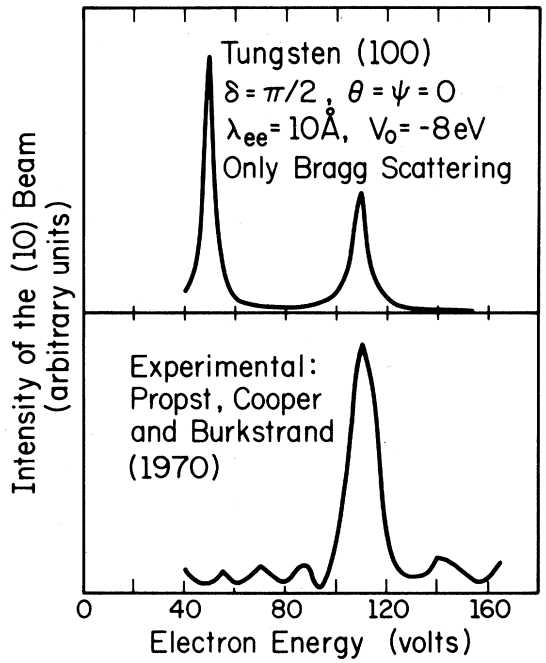

FIG. 1. Elastic scattering from $W(100)$ for the (10) beam. An inner potential of $V_0 = -8$ eV is used to place a kinematical Bragg peak in the theoretical calculation at the position of a prominent peak in the experimental data. The experimental work comes from Ref. 20.

of model calculations of the diffracted intensity using the forms for M associated with various models defined in I.

III. EXCITATION OF BULK LOSS MODES

A. Model Description

In this section we investigate the systematics of inelastic electron diffraction when a "bulk" (i.e., propagating or standing-wave) excitation is created in the sample. For simplicity we initially neglect lifetime effects, and take the zero-temperature limit. In this case

$$-2iN(-w)\,\mathrm{Im}D(\vec{p},w) = 2\pi\delta(w-\hbar\omega(\vec{p}))\ . \tag{3.1}$$

Substituting Eq. (3.1) into Eq. (2.1) we use the momentum-conservation δ function to perform the integral over $\vec{p}_{\parallel}$, then use the energy δ function of Eq. (3.2) to perform the integral over $p_{\perp}$. Assuming a symmetric dispersion relationship for the excitation, the result of this integration is given by

$$\frac{d^2\sigma}{dEd\Omega} = \left(\frac{E-w}{E}\right)^{1/2}\frac{1}{(2\pi)^3 A}\sum_{\vec{g}}\rho(w,\vec{p}^{\,0}_{\parallel})$$
$$\times\left[M(k_{\perp}(0,E),k'_{\perp}(0,E-w),p^0_{\perp},\vec{g})\right.$$
$$\times\left|A_b(\vec{g},p^0_{\perp},E,w)+A_c(\vec{g},p^0_{\perp},E,w)\right|^2$$
$$+M(k_{\perp}(0,E),k'_{\perp}(0,E-w),-p^0_{\perp},\vec{g}$$
$$\left.\times\left|A_b(\vec{g},-p^0_{\perp},E,w)+A_c(\vec{g},-p^0_{\perp},E,w)\right|^2\right]\ . \tag{3.2}$$

In Eq. (3.2) $\vec{p}^{\,0}_{\parallel}$ is specified by

$$\vec{p}^{\,0}_{\parallel} = \vec{k}_{\parallel}+\vec{g}-\vec{k}'_{\parallel}\ ; \tag{3.3a}$$

$p^0_{\perp}$ is defined through

$$\hbar\omega(\vec{p}^{\,0}_{\parallel},p^0_{\perp}) = w; \tag{3.3b}$$

and $\rho(w,\vec{p}^{\,0}_{\parallel})$ is a density-of-states factor

$$\rho(w,\vec{p}^{\,0}_{\parallel}) = \left|\frac{\partial\hbar\omega(\vec{p})}{\partial p_{\perp}}\right|^{-1}_{\vec{p}_{\parallel}=\vec{p}^{\,0}_{\parallel},\,\hbar\omega=w}\ . \tag{3.3c}$$

Equation (3.2) holds provided the solution of Eq. (3.3b) yields a real $p^0_{\perp}$. Otherwise $d^2\sigma/dEd\Omega = 0$.

For simplicity in this section we restrict our considerations to the case of an isotropic quadratic dispersion relation for the loss mode

$$\hbar\omega(\vec{p}) = \alpha_q p^2+\hbar\omega_{bq}\ . \tag{3.4}$$

For this form of the dispersion relation

$$\rho_q(w,\vec{p}^{\,0}_{\parallel}) = (2\alpha_q p^0_{\perp})^{-1} \tag{3.5}$$

which diverges as $p^0_{\perp}\to 0$.

We choose the geometrical parameters so that the solid corresponds to W[100], and consider the case of only primary Bragg scattering at the elastic scattering vertex.[18] The value of the inner potential has been chosen to place a primary Bragg peak at the position where a prominent peak appears in the experimental data for the (10) beam[20] as illustrated in Fig. 1. Within the framework of the s-wave model[18] this can be thought of as a shift of the energy band gap corresponding to the (10) reflection to the observed position on the energy scale. The loss modes in tungsten are not known and, even with multiple scattering, the s-wave model does not give very good agreement with the experimental elastic scattering data for tungsten.[5,20] Therefore, it does not seem advisable to proceed beyond this rough model at the present. However, the model is adequate for the exploration of systematic features of inelastic diffraction.

In Sec. III B we investigate inelastic diffraction in the (00) beam using the two "schematic" models for the coupling to the loss mode[1-3]

$$U = 1\ \text{eV Å}^{9/2}\,\theta(p_m-p) \tag{3.6a}$$

and

$$U = p_{\perp}\ \text{eV Å}^{11/2}\,\theta(p_m-p)\ , \tag{3.6b}$$

where p_m is a cutoff momentum and

$$\theta(p_m-p) = \begin{cases} 1 & \text{for } p_m \geq p \\ 0 & \text{for } p_m \leq p \end{cases}\ . \tag{3.6c}$$

The vertices specified in Eqs. (3.6a) and (3.6b) have the dimensions of eV Å$^{9/2}$. Hence, in Eq.

(3.6b) $p_\perp$ is to be specified in Å^{-1}. We shall see that these two couplings give rise to quite different angular profiles. Then in Sec. III C we examine inelastic diffraction in the (10) beam.

B. Inelastic Diffraction in the (00) Beam

1. *Constant Coupling Vertex*

In this section we use the coupling vertex given in Eq. (3.6a). It is the prototype for vertices which *do not* go to zero as $p_\perp \to 0$ sufficiently fast to overcome the density-of-states singularity. Evaluation of the quantity M in Eq. (3.2) yields[1]

$$M(k_\perp(0,E), k_\perp'(0,E-w), p_\perp^0, \vec{g}) = (m/\hbar^2)^4 (1/A^2) \times |1 - R(k_\perp(0,E), k_\perp'(0,E-w), -p_\perp^0, \vec{g})|^{-2}, \quad (3.7)$$

where A is the area of a unit cell of the surface. Thus Eqs. (2.3)–(2.8), (3.2), (3.3), and (3.7) specify the two-step inelastic cross section for this model.

a. Energy profiles. A resonance in the A_b term in Eq. (3.2) occurs when

$$2\mathrm{Re}[k_\perp(0,E)] = 2\pi n/d, \quad (3.8)$$

where n is an integer. This is the condition for a Bragg resonance at energy $E = E_B$ in the elastic channel. Hence, this resonance produces an image in the inelastic energy profile of the kinematical Bragg peak in the elastic intensity profile. Note that the value of $p_\perp$ can have essentially no effect on this resonance since from Eq. (2.3) the quantity

$$F_b(p_\perp) = \frac{R[k_\perp'(0,E-w), -k_\perp(\vec{g},E), -p_\perp; 0] - 1}{i[k_\perp'(0,E-w) - k_\perp(\vec{g},E) - p_\perp]\, d} \quad (3.9)$$

is large only for forward scattering at the inelastic vertex, i.e., $[k_\perp'(0,E-w) - k_\perp(\vec{g},E) - p_\perp] \to 0$. In this case $F_b(p_\perp) \to 1$ so that no additional resonance occurs. Similarly, the resonance condition in the A_c term occurs when

$$2\mathrm{Re}[k_\perp(0,E-w)] = 2\pi m/d, \quad (3.10)$$

which is the condition for a Bragg resonance at energy $E = (E_B + w)$ in the elastic channel. This resonance also is essentially independent of $p_\perp$.

The A_b and A_c resonances are the energy-tuned resonances in the inelastic channel.

The envelope functions M, which occur in Eq. (3.2) and are specified by Eq. (3.7), exhibit kinematical resonances at energies such that

$$\mathrm{Re}[k_\perp(0,E) + k_\perp'(0,E-w)] - p_\perp^0 = 2\pi n/d \quad (3.11a)$$

or

$$\mathrm{Re}[k_\perp(0,E) + k_\perp'(0,E-w)] + p_\perp^0 = 2\pi n/d. \quad (3.11b)$$

The resonance condition in Eq. (3.11b) occurs somewhere near the A_b resonance. For relatively large values of $p_\perp^0$ the resonance occurs at a lower energy than the A_b resonance, but for small values of $p_\perp^0$ the resonance will lie between the A_b and A_c resonances. On the other hand the resonance condition in Eq. (3.11a) occurs somewhere near the A_c resonance. For relatively large values of $p_\perp^0$ this resonance occurs at a higher energy than the A_c resonance, but for small values of energy the resonance lies between the A_b and A_c resonances.

These resonances in M constitute the momentum-tuned "sideband-diffraction" resonances.[2] They can cause each of the energy-tuned resonant peaks to split into two peaks. Thus we can find *four* peaks in the inelastic energy profile corresponding to each peak in the elastic energy profile. This further splitting is especially evident for a "steep" dispersion relation where a large $p_\perp^0$ corresponds to a fairly large loss energy w. We illustrate the effect for such a "steep" dispersion relation in Fig. 2. This is for the special case of specular reflection for a normally incident beam, i.e., $\vec{p}_\parallel^{\,0} = 0$. The elastic profile is shown in Fig. 2(a). With only primary Bragg scattering at the elastic vertex, it consists only of two primary Bragg peaks—one at $E = 23$ eV and one at $E = 68$ eV. Note that for very small losses [Fig. 2(b)], $p_\perp^0$ cannot become large enough to tune the sideband-diffraction resonance. In this case we see only the two energy-tuned resonances. For larger losses [Figs. 2(c) and 2(d)], the additional sideband-diffraction resonances are quite evident.

b. Angular profiles. The features of the angular profiles are determined primarily by the product of the envelope function and the density of states, i.e.,

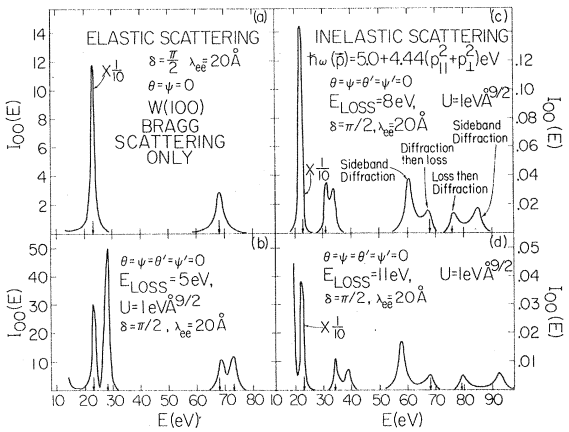

FIG. 2. Energy profiles obtained for elastic (a) and inelastic (b)–(d) diffraction using only primary Bragg scattering at the elastic vertex. The inelastic profiles were calculated using Eqs. (3.2) and (3.7) of the text and the parameters shown in the figure. The large value of λ_{ee} is used only for illustrative pruposes.

$$F_{\pm}(p_{\perp}^{0}) \equiv \frac{M(k_{\perp}(0,E), k_{\perp}'(0,E-w), \mp p_{\perp}^{0}, 0)}{2\alpha_q p_{\perp}^{0}} \ . \quad (3.12)$$

Let us consider the case of normal incidence $\theta \equiv 0$ and constant azimuthal angle along one of the principal axes in the plane, i.e., $\psi = \psi' = 0$. In terms of the final angle θ' the various momenta are given by

$$k_{\perp}'(E-w) = k(E-w)\cos\theta' \ , \quad (3.13a)$$

$$k_{\parallel}'(E-w) = k(E-w)\sin\theta' \ , \quad (3.13b)$$

$$\vec{p}_{\parallel}^{\,0} = -\vec{k}_{\parallel}'(E-w) \ . \quad (3.13c)$$

From the dispersion relation we obtain the expression for $p_{\perp}^{0}$

$$p_{\perp}^{0} = \left(\frac{(w-\hbar\omega_{bq})}{\alpha_q} - k^2(E-w)\sin^2\theta' \right)^{1/2} \ . \quad (3.14)$$

From Eq. (3.14) we see that we can obtain a nonzero scattering intensity out to a critical angle θ_c' given by

$$\theta_c' = \arcsin\left[\left(\frac{w-\hbar\omega_{bq}}{\alpha_q k^2(E-w)} \right)^{1/2} \right] \ . \quad (3.15)$$

At this critical angle $p_{\perp}^{0} = 0$. The position of the critical angle as a function of w gives a measure of $\hbar\omega(\vec{p}_{\parallel})$ since $\hbar\omega(p_{\parallel}^{\max}) = w$ at the critical angle. As $F_{\pm}(p_{\perp}^{0})$ diverges at $p_{\perp}^{0} \to 0$, we anticipate a sharp increase in the diffracted intensity as $\theta' \to \pm\theta_c'$. This effect should be especially evident for values of the incident electron's energy which are far removed from any peaks in the energy profile. We illustrate this phenomenon in Fig. 3 in which we display angular profiles for various energy losses for a primary beam energy 10 eV below the Bragg energy.

We next examine the case where sweeping through $p_{\perp}^{0}$ in the angular profile produces a sideband-diffraction resonance. This will occur near an incident beam energy for which there is a peak in the

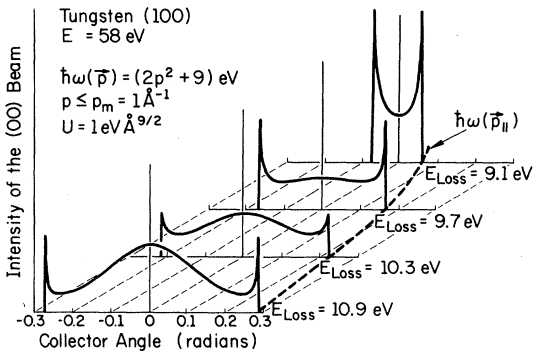

FIG. 3. Angular profiles for various loss energies. The energy of the incident beam is 10 eV below the energy of Bragg peak. The profiles were calculated using Eqs. (3.2) and (3.7) of the text, $\lambda_{ee} = 10$ Å, $\theta = \psi = \psi' = 0$, and the parameters shown in the figure. The critical cutoff angle maps out $\hbar\omega(p_{\parallel})$ as shown by the dotted line.

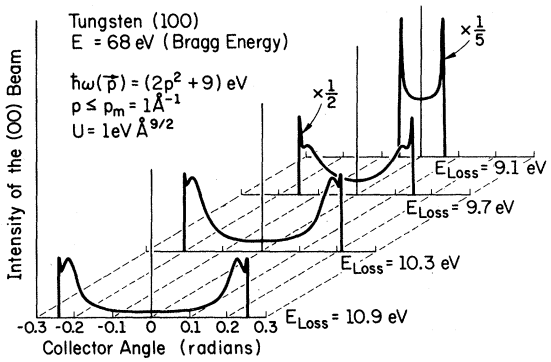

FIG. 4. Angular profiles for various loss energies the energy of the incident beam is equal to the Bragg energy. The profiles were calculated using Eqs. (3.2) and (3.7) of the text, $\lambda_{ee} = 10$ Å, $\theta = \psi = \psi' = 0$, and the parameters shown in the figure.

energy profile. The sideband-diffraction resonance will produce maxima in the angular profiles in addition to those associated with the density-of-states effect at $\theta' = \theta_c$. We illustrate this effect in Fig. 4 for the case of a primary beam energy equal to the kinematical Bragg energy. Note the additional peaks in the angular profiles when the loss energy becomes large enough to allow $p_{\perp}^{0}$ to tune the resonance. These peaks are associated with a local maximum in $F_{+}(p_{\perp}^{0})$ which is associated with the resonance condition given by Eq. (3.11b). For a primary beam energy $E \simeq E_B + w$ we also would obtain additional peaks in the angular profiles. In this case the peaks would be associated with a local maximum in $F_{-}(p_{\perp}^{0})$ [resonance condition Eq. (3.11a)].

In calculating the profiles shown in Figs. 3 and 4 we have used a more realistic "flat" loss-mode dispersion relation. Even for such a "flat" dispersion relation, the effects of sideband diffraction are still apparent in the angular profiles. This is because in an angular profile $p_{\perp}^{0}$ is swept through its entire allowed range.

2. *Coupling Vertex Proportional to* $p_{\perp}$

In this section we use the coupling vertex given in Eq. (3.6b). It is the prototype for vertices which vanish at $p_{\perp} \to 0$ sufficiently rapidly to overcome the density-of-states singularity. This coupling vertex duplicates the essential features of the semi-infinite jellium-model vertex for coupling to bulk plasmons.[1,4,17] Evaluation of the quantity M yields

$$M(k_{\perp}(0,E), k_{\perp}'(0,E-w), p_{\perp}^{0}, \vec{g}) = (m/\hbar^2)^4 [(p_{\perp}^{0})^2/A^2] \times \left| 1 - R(k_{\perp}(0,E), k_{\perp}'(0,E-w), -p_{\perp}^{0}, \vec{g}) \right|^{-2} \ . \quad (3.16)$$

a. Energy profiles. The form of the coupling can have no effect on A_b and A_c in Eq. (3.2) so the two energy-tuned resonances occur as before when Eqs. (3.8) and (3.10) are satisfied. Also the factor

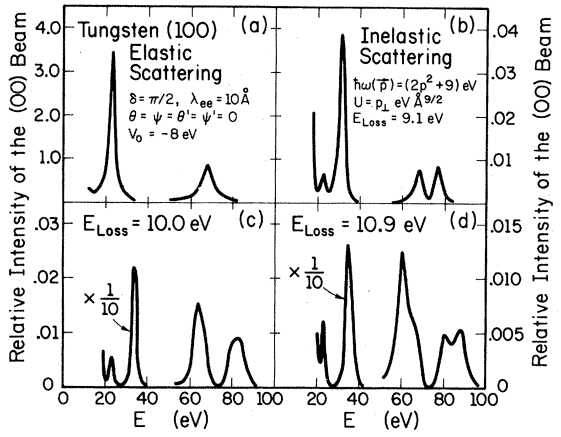

FIG. 5. Energy profiles obtained for elastic (a) and inelastic (b)–(d) diffraction using only primary Bragg scattering at the elastic vertex. The inelastic profiles were calculated using Eqs. (3.2) and (3.16) of the text and the parameters shown in the figure.

of $(p_\perp^0)^2$ in the numerator of Eq. (3.16) has little effect on the resonance condition for the envelope function. Hence, the momentum-tuned resonances occur when Eqs. (3.11) are satisfied.

We again examine energy profiles for case of specular reflection of a normally incident beam. In this case for a given loss energy only a constant scaling factor relates the profiles for this coupling to the profiles for constant coupling. Thus, the energy profiles for the two different couplings are directly comparable. We show calculated energy profiles in Fig. 5 for the case of a fairly "flat" dispersion curve. The elastic energy profile is shown in Fig. 5(a). The extra sideband-diffraction resonances appear distinctly only for the largest loss energy, i.e., in Fig. 5(d). This result is due to the "flatness" of the dispersion relation. Furthermore as the detector is moved away from the specular direction and requires a nonzero $p_\parallel^0$, the value of $p_\perp^0$ for a given loss will be less than when $\theta' = 0$. This further reduces the ability of the envelope function to resonate and produce sideband-diffraction peaks. We illustrate this effect in Fig. 6, where we look at the structure above 50 eV in Fig. 5(d) as a function of θ'. Note the disappearance of the sideband-diffraction peaks with increasing θ'. For the case of bulk plasmons where a flat dispersion curve combines with lifetime effects[1–4] it is difficult to see sideband-diffraction phenomena in the energy profiles—especially when multiple elastic scattering effects are included in the calculation.

b. Angular profiles. The features of the angular profiles again are largely determined by the product of the envelope function and the density of states

$$G_\pm(p_\perp^0) = \frac{M(k_\perp(0, E), k_\perp'(0, E - w), \mp p_\perp^0, 0)}{2\alpha_q p_\perp^0}, \quad (3.17)$$

where M is given by Eq. (3.16). Unlike $F_\pm(p_\perp^0)$, $G_\pm(p_\perp^0)$ does not diverge as $p_\perp^0 \to 0$ but rather behaves according to

$$G_\pm(p_\perp^0) = 0 \text{ as } p_\perp^0 \to 0 . \quad (3.18)$$

Hence, the scattered intensity goes to zero in a smooth manner at $\theta' \to \theta_c$. The angular profiles for incident electron energies far removed from those of peaks in the energy profile reflect the behavior of $G_\pm(p_\perp^0)$. This result is evident from Fig. 7 where we display angular profiles for various energy losses for a primary beam energy 10 eV below the Bragg energy.

We next consider angular profiles when the incident beam energy is near the energy for which there is a peak in the energy profile. Sweeping through $p_\perp^0$ in the angular profile produces sideband-diffraction resonances provided that the loss is sufficiently large to allow $p_\perp^0$ to tune the resonance. We illustrate this effect in Fig. 8. For the lowest loss energy $p_\perp^0$ cannot become large enough to tune the resonance, and we see only a singlet structure such as that shown in Fig. 7. However, for larger values of the loss energies we see the characteristic doublet caused by the sideband-diffraction resonances.

From the difference between Figs. 7 and 8 it is clear that for incident electron energies in the vicinity of a resonance in the elastic LEED cross section, the angular profiles are quite sensitive to the beam energy. This result is illustrated more directly in Fig. 9 in which we show the dependence of the angular profiles (for a given loss energy) upon the energy of the incident beam. We have chosen a loss energy large enough for the angular profiles to exhibit the sideband-diffraction reso-

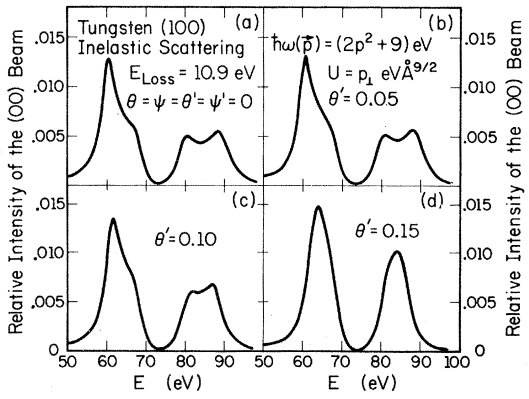

FIG. 6. Inelastic energy profiles showing the effect of moving the detector off the specular direction. The profiles were calculated using Eqs. (3.2) and (3.16) of the text and the parameters shown in the figure.

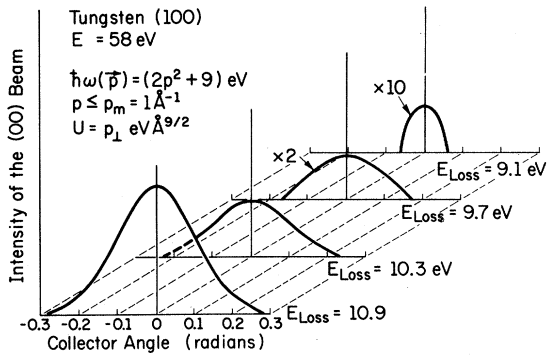

FIG. 7. Angular profiles for various loss energies. The energy of the incident beam is 10 eV below the energy of the Bragg peak. The profiles were calculated using Eqs. (3.2) and (3.16) of the text, $\lambda_{ee}=10$ Å, $\theta=\psi=\psi'=0$, and the parameters shown in the figure.

nances. Note the characteristic shift from a singlet to a doublet and then back to a singlet as the beam energy goes over a peak in the inelastic energy profile. The inelastic energy profile in Fig. 5(c) corresponds to the loss energy used here. The sideband-diffraction effects are quite apparent in the angular profiles even though they are not evident in the energy profile.

c. Loss profiles. In general the energy of the incident beam is much larger than the loss energy w. Also the loss energy varies only over a relatively small range. These facts have the consequences that for fixed incident and final angles and fixed primary beam energy, $k_\perp(0,E)$ is fixed and $k_\perp(0,E-w)$ will be only a slowly varying function of w. Thus both A_b and A_c will vary slowly as w ranges over a small range and any structure in the loss profile will be due to the envelope function M.

Let us examine the case of specular reflection of a normally incident beam, i.e., $\vec{p}_{\parallel}^{\,0}=0$. The loss energy is given by

$$w=\hbar\omega_{bq}+\alpha_q(p_\perp^0)^2=\hbar\omega_{bq}+\Delta w\ , \tag{3.19}$$

from which we obtain

$$p_\perp^0=(\Delta w/\alpha_q)^{1/2} \tag{3.20}$$

and

$$\mathrm{Re}[k_\perp'(0,E-w)]\simeq\{(2m/\hbar^2)\times[(E+V_0-\hbar\omega_{bq})-\Delta w]\}^{1/2}\ . \tag{3.21}$$

We first consider the situation in which the incident beam energy is below the Bragg energy. In this case we find

$$\mathrm{Re}[k_\perp(0,E)+k_\perp'(0,E-w)]<2\mathrm{Re}[k_\perp(0,E_B)]=2\pi\bar{n}/d\ , \tag{3.22}$$

where $\bar{n}$ is some particular integer. We note that since $(E-\hbar\omega_{bq}+V_0)\gg\Delta w$, $p_\perp^0$ will increase faster with increasing Δw than $k_\perp'(0,E-w)$ will decrease. This fact results in a net increase of $\mathrm{Re}[k_\perp(0,E)+k_\perp'(0,E-w)+p_\perp^0]$ with increasing Δw. Hence, sweeping Δw will yield a peak in the loss profile when

$$\mathrm{Re}[k_\perp(0,E)+k_\perp'(0,E-w)+p_\perp^0]=2\pi\bar{n}/d \tag{3.23}$$

is satisfied for some Δw.

As we increase E, a smaller value of Δw will be required to satisfy Eq. (3.23), and the peak in the loss profile will shift to lower values of w. This trend continues until we reach an incident beam energy E_1 such that

$$\mathrm{Re}[k_\perp(0,E_1)+k_\perp'(0,E_1-\hbar\omega_{bq})]=2\pi\bar{n}/d\ . \tag{3.24}$$

At this point the resonance condition specified by Eq. (3.23) is satisfied for $p_\perp^0=0$, and the peak in the loss profile will be very close to $\Delta w=0$. The peak can never be exactly at $\Delta w=0$ with this coupling since we have zero intensity at $p_\perp^0=0$.

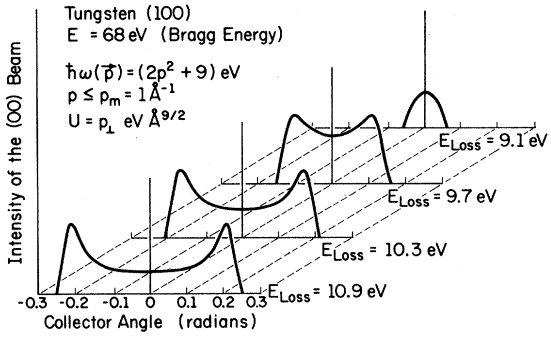

FIG. 8. Angular profiles for various loss energies. The energy of the incident beam is equal to the Bragg energy. The profiles were calculated using Eqs. (3.2) and (3.16) of the text, $\lambda_{ee}=10$ Å, $\theta=\psi=\psi'=0$, and the parameters shown in the figure.

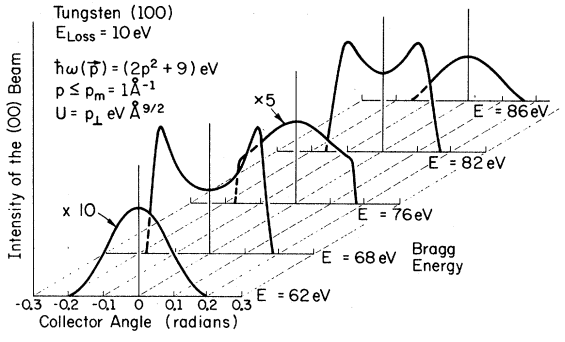

FIG. 9. Inelastic angular profiles associated with a loss energy of 10 eV for an incident beam whose energy is noted in the various panels of the figure. The profiles were calculated using Eqs. (3.2) and (3.16) of the text, $\lambda_{ee}=10$Å, $\theta=\psi=\psi'=0$, and the parameters shown in the figure.

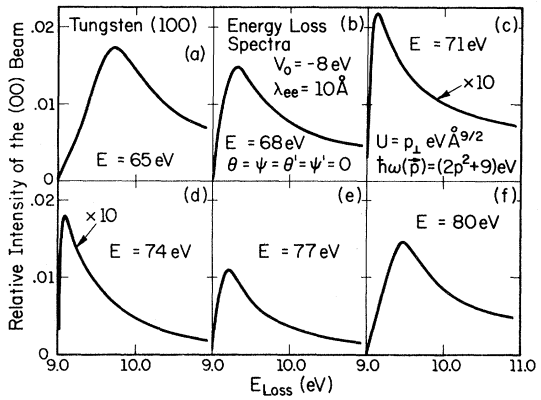

FIG. 10. Inelastic loss profiles as a function of incident beam energy for the case of a specularly reflected normally incident beam. The profiles were calculated using Eqs. (3.2) and (3.16) of the text and the parameters shown in the figure.

For $E > E_1$ we find

$$\mathrm{Re}[k_\perp(0,E) + k_\perp'(0,E-w)] > 2\pi\bar{n}/d \ . \qquad (3.25)$$

Therefore the only possible resonance occurs when

$$\mathrm{Re}[k_\perp(0,E) + k_\perp'(0,E-w) - p_\perp^0] = 2\pi\bar{n}/d \ . \qquad (3.26)$$

With increasing values of E this condition will require increasingly larger values of $p_\perp^0$ and hence of Δw. The peak in the loss profile will thus begin to move out to higher values of the loss energy.

Starting with $E < E_B$, as E increases the systematic behavior of the peak in the loss profile moving from some fairly large value of Δw, in to $\Delta w \simeq 0$, and then back out to large Δw again is illustrated in Fig. 10. This type of behavior of the loss profile is evident in early experimental work of Farnsworth *et al.*[8,9] although it is displayed more prominently in recent experiments.[21,22]

We also note that when Eq. (3.24) is satisfied, we are midway between the two energy-tuned A_b and A_c resonances. This results in a minimum in $|A_b + A_c|^2$ and hence we expect an over-all decrease in the intensity of the loss profile as the peak position approaches $\Delta w = 0$. Such an effect is evident in panels (c) and (d) of Fig. 10.

C. Inelastic Diffraction in the (10) Beam

The same general sort of resonance conditions hold for $\vec{g} \neq 0$ as occur for $\vec{g} = 0$. Specifically, these conditions are given by (i) A_b resonance:

$$\mathrm{Re}[k_\perp(0,E) + k_\perp(\vec{g},E)] = (2\pi m/d) - \vec{g}\cdot\vec{a}/d \ ; \ (3.27a)$$

(ii) A_c resonance:

$$\mathrm{Re}[k_\perp'(0,E-w) + k_\perp'(-\vec{g},E-w)] = (2\pi m/d) - \vec{g}\cdot\vec{a}/d \ ; \qquad (3.27b)$$

(iii) $M(k_\perp(0,E),\ k_\perp'(0,E-w),\ p_\perp^0, \vec{g})$ sideband-diffraction resonance:

$$\mathrm{Re}[k_\perp(0,E) + k_\perp'(0,E-w) - p_\perp^0] = (2\pi m/d) - \vec{g}\cdot\vec{a}/d \ ; \qquad (3.27c)$$

(iv) $M(k_\perp(0,E),\ k_\perp'(0,E-w),\ -p_\perp^0, \vec{g})$ sideband-diffraction resonance:

$$\mathrm{Re}[k_\perp(0,E) + k_\perp'(0,E-w) + p_\perp^0] = (2\pi n/d) - \vec{g}\cdot\vec{a}/d \ . \qquad (3.27d)$$

However, the quantitative details in the profiles produced by these resonances can be quite different from those in the $\vec{g} \neq 0$ case.

1. *Energy Profiles*

The inelastic energy profiles taken at fixed θ' show the same general characteristics as those for the (0, 0) beam with the addition of several complicating features.

(i) The angular position of the $\vec{p}_\parallel^{\,0} = 0$ point now varies with the energy of the incident beam even when the incident beam is normally incident. This is because adding $\vec{g}_{10}$ to an initial wave vector shifts the final wave vector to larger values of θ' with the amount of the shift being energy dependent. We have a similar situation for a beam not at normal incidence even when $\vec{g} = 0$ because when the electron has lost energy $\vec{k}_\parallel' = \vec{k}_\parallel \neq 0$ no longer corresponds to specular reflection.

(ii) For fixed θ' the size of the $p_\perp^0$ therefore depends on E as well as w. This affects the details of the peak splitting in the energy profiles although the general features will be the same as for the (00) beam.

(iii) The loss energy w limits the maximum value of $p_\parallel^0$ and hence the range of θ' for which we obtain scattered intensity for a given energy E. When too large a value of $p_\parallel^0$ is needed to place the beam at the specified θ', the inelastic energy profile will cut off. This can happen at both low and high energies.

We do not illustrate further these effects in figures because they occur in the semiquantitative calculations for Al as shown in Sec. V which are performed for a beam at non-normal incidence.

2. *Loss Profiles*

The loss profiles also are complicated by the shift in angle of the $\vec{p}_\parallel^{\,0} = 0$ point as w changes for fixed E. Increasing the loss energy moves the $\vec{p}_\parallel^{\,0} = 0$ point to higher values of θ'. However, as the variation of w will be small compared to a typical $E' = E - w$, this motion does not affect the loss substantially. The loss profiles look much like those for the (00) beam if they are taken at a θ' near the value where $\vec{p}_\parallel^{\,0} = 0$. If on the other hand, the loss profiles are taken at an angle θ' where $\vec{p}_\parallel^{\,0}$ is large (implying only small values of $p_\perp^0$ occur), the resonance peaks in the loss profile will not show a pro-

nounced movement with changing incident beam energy. Also in this case the loss energy cannot vary over as wide a range as before since we clearly must have $\Delta w \geq \alpha_q (p_{\parallel}^0)^2$.

3. *Angular Profiles*

In the case of the (10) beam we do not expect the angular profiles to be symmetric about the angle θ_0', where $\vec{p}_{\parallel}^{\,0} = 0$. Broadly speaking, this asymmetry occurs because the sine and cosine functions do not have the symmetry about a general θ_0' that they do about $\theta_0' = 0$.

For the sake of discussion let us consider the case of a normally incident beam and the coupling given by Eq. (3.6b) for which the angular profiles go to zero when $p_{\perp}^0 \to 0$. In order to isolate the dependence on the collector angle, we rewrite the resonance conditions in Eqs. (3.27) in terms of θ'. These become for the (100) faces of monatomic fcc and bcc metals, (i) A_b resonance (independent of θ'):

$$\mathrm{Re}\{k(E) + [k^2(E) - g_{10}^2]^{1/2}\} = (2n+1)\pi/d \; ; \quad (3.28a)$$

(ii) A_c resonance:

$$\mathrm{Re}\big(k(E-w)\cos\theta' + \{k^2(E-w) - [k(E-w)\sin\theta' - g_{10}]^2\}^{1/2}\big) = (2n+1)\pi/d \; ; \quad (3.28b)$$

(iii) $M(k_{\perp}(0,E), k_{\perp}'(0,E-w), p_{\perp}^0, \vec{g}_{10})$ sideband-diffraction resonance:

$$J_{10}^{-} \equiv \mathrm{Re}\big(k(E) + k(E-w)\cos\theta' - \{(w-\hbar\omega_{bq})\alpha_q - [k(E-w)\sin\theta' - g_{10}]^2\}^{1/2}\big) = (2n+1)\pi/d \; ; \quad (3.28c)$$

(iv) $M(k_{\perp}(0,E), k_{\perp}'(0,E-w), -p_{\perp}^0, \vec{g}_{10})$ sideband-diffraction resonance:

$$J_{10}^{+} \equiv \mathrm{Re}\big(k(E) + k(E-w)\cos\theta' + \{(w-\hbar\omega_{bq})/\alpha_q - [k(E-w)\sin\theta' - g_{10}]^2\}^{1/2}\big) = (2n+1)\pi/d \; . \quad (3.28d)$$

In writing Eqs. (3.28) we have made use of the fact that for the (100) faces of fcc and bcc metals

$$\vec{g}_{10} \cdot \vec{a}/d = \pi/d \; . \quad (3.29)$$

In analogy with our analysis for the (00) beam, let us consider how we expect the angular profiles for a fixed loss energy to behave as we change the energy of the incident beam. When $E \ll E_B$ we expect a singlet structure due to the product ρM. Although no longer symmetric, this singlet will be "centered" near $\theta' = \theta_0'(E)$. With increasing incident beam energy, the J_{10}^{+} resonance will become important. This resonance will occur first at the value of θ' that maximizes J_{10}^{+}. Due to the $k(E-w)\times\cos\theta'$ term in Eq. (3.28d), this will occur at a θ' somewhat less than $\theta_0'(E)$. Further increase of E will cause a doublet to form which will separate with increasing incident beam energy. However, there will be no symmetry developed about $\theta_0'(E)$. We can see this as follows, from Eq. (3.28d):

$$\Delta J_{10}^{+} = -\Delta\theta' \,\mathrm{Re}\Big(k(E-w)\sin\theta' + \frac{k(E-w)\cos\theta'[k(E-w)\sin\theta' - g_{10}]}{\{(w-\hbar\omega_{bq})/\alpha_q - [k(E-w)\sin\theta' - g_{10}]^2\}^{1/2}}\Big) . \quad (3.30)$$

The second term on the right-hand side of Eq. (3.30) may be rewritten as

$$\mathrm{Re}\Big(\frac{k(E-w)\cos\theta[k(E-w)\sin\theta' - g_{10}]}{\{(w-\hbar\omega_{bq})\alpha_q - [k(E-w)\sin\theta' - g_{10}]^2\}^{1/2}}\Big) = \frac{\mathrm{Re}[k(E-w)]\cos\theta' p_{\parallel}^0}{[(w-\hbar\omega_{bq})/\alpha_q - (p_{\parallel}^0)^2]^{1/2}} \; . \quad (3.31)$$

This term is greater than zero for $\theta' > \theta_0'(E)$ (i.e., $p_{\parallel}^0 > 0$) but is less than zero for $\theta' < \theta_0'(E)$ (i.e., $p_{\parallel}^0 < 0$). This term dominates in Eq. (3.30) causing the splitting into two resonant peaks. However, since $[\mathrm{Re}k(E-w)\sin\theta_0'(E)] \neq 0$, the two peaks do not move at equal rates away from $\theta = \theta_0'(E)$. Because of these resonances and also the growth of the A_b term, we expect the over-all size of the angular profile to increase with the onset of the doublet structure.

As E passes through the Bragg energy, the next resonance that occurs is the onset of the low-angle peak in the J_{10}^{-} resonance. At the extreme ends of the profile $p_{\perp}^0 = 0$, but offsetting this is the fact that $\mathrm{Re}k(E-w)\cos\theta'$ takes on its maximum value at the low-angle end. Hence for some $E > E_B$ the low-angle end of the doublet becomes much larger than the high-energy end because of the resonance in both J_{10}^{+} and J_{10}^{-}.

Increasing E still further causes the low-angle end of the J_{10}^{-} resonance to move towards $\theta_0'(E)$ and the low-angle end of the J_{10}^{+} resonance to disappear. We thus obtain a singlet structure towards the low-angle side of the profile.

The A_c resonance is the next to enter the picture. From Eq. (3.28b) we see that this resonance first occurs at the low-angle end of the profile. In general it will give a singlet peak moving to higher energies with increasing incident beam energy. With still further increase of E, the A_c peak and the low-angle J_{10}^{-} resonance separate, and we obtain a doublet structure.

Summarizing, with E increasing from a value well below the Bragg energy, we expect the following behavior in the angular profile: We first obtain a small singlet which then changes into a much larger doublet with the two peaks being about the same

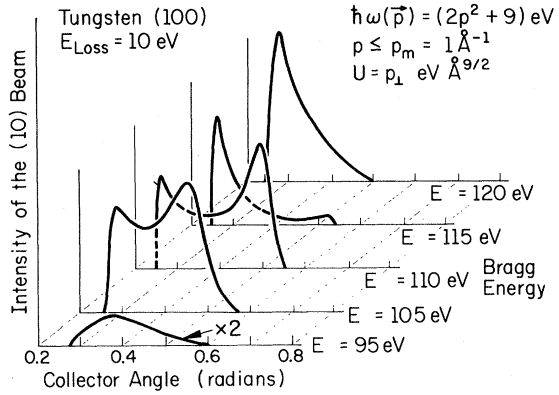

FIG. 11. Inelastic angular profiles for the (10) beam for the case of a normally incident beam. The energy of the incident beam is noted in the various panels of the figure. The profiles were calculated using Eqs. (3.2) and (3.16) of the text and the parameters shown in the figure.

size. The high-angle member of the doublet will then decrease in size relative to the low-angle member. Eventually, at some $E < (E_B + w)$, we will see only a single peak towards the low-angle side of the profile. Further increase of E will cause the singlet to split into a doublet which will finally go back into a small singlet when E is well beyond any structure in the energy profile. This systematic behavior is exhibited in Fig. 11. At $E = 125$ eV (not shown in the figure) the doublet structure reappears as expected.

IV. EXCITATION OF SURFACE LOSS MODES

In this section we discuss the characteristic features of inelastic diffraction when a "surface" excitation is created in the sample. We can immediately perform the momentum integral in Eq. (2.1) to obtain

$$\frac{d^2\sigma}{dEd\Omega} = \left(\frac{E-w}{E}\right)^{1/2} \times \frac{1}{(2\pi)^3 A} \sum_{\vec{g}} [-2iN(-w)\mathrm{Im}D(\vec{p}_\parallel^{\,0}, w)] \times M(k_\perp(0,E), k_\perp'(0,E-w), p_\perp(\vec{p}_\parallel^{\,0}), \vec{g}) \times |A_b(\vec{g}, p_\perp(\vec{p}_\parallel^{\,0}), E, W) + A_c(\vec{g}, p_\perp(\vec{p}_\parallel^{\,0}), E, W)|^2 , \quad (4.1)$$

where $\vec{p}_\parallel^{\,0}$ is given by Eq. (3.3a) and $p_\perp(\vec{p}_\parallel^{\,0})$ is a specified function of $\vec{p}_\parallel^{\,0}$ that depends on the particular kind of surface excitation involved.

Suppose the surface excitation is an exact eigenstate of the system. This would mean that (taking the $T = 0$ limit)

$$-2iN(-w)\mathrm{Im}D(\vec{p}_\parallel^{\,0}, w) = 2\pi\delta(w - \hbar\omega(\vec{p}_\parallel^{\,0})) . \quad (4.2)$$

Note that the energy δ function in Eq. (4.2) is nonzero only for certain special (real) values of $p_\parallel^0$. That is, there will be only certain directions for which we can simultaneously satisfy conservation of both energy and parallel momentum. It is only for these special directions that we obtain a nonzero diffraction intensity for a given energy loss. For a symmetric dispersion relation and fixed azimuthal angle $\psi = \psi'$, there will be two values of $\vec{p}_\parallel^{\,0}$ for which Eq. (4.2) is satisfied. Therefore, in general there will be two final angles θ' for which there will be a nonzero diffracted intensity for a given energy loss. Assuming infinite instrumental resolution, an angular profile for a given reciprocal-lattice vector $\vec{g}$ would always show two spikes [provided that a real nonzero value of $|\vec{p}_\parallel^{\,0}|$ satisfies Eq. (4.2)] associated with the intersection of the scattering plane with a cone of inelastically scattered electrons. The intensity of these spikes would be determined by the other quantities in Eq. (4.1). In an actual experimental measurement, the observed profiles would depend on the angular acceptance cone and the accepted energy width for the measuring instrument.

In practice, however, no surface excitation is an exact eigenstate of the system. Consequently, the spectral density is given by

$$-2iN(-w)\,\mathrm{Im}D(\vec{p}_\parallel^{\,0}, w) = 2\Gamma / \{[w - \hbar\omega(\vec{p}_\parallel^{\,0})]^2 + \Gamma^2\} , \quad (4.3)$$

in which Γ is some intrinsic width due to the finite lifetime of the excitation, and we have taken the $T \to 0$ limit. Unlike the situation for bulk excitations, for nonzero $\vec{p}_\parallel^{\,0}$, a surface excitation always can decay into a single electron-hole pair.[16] This is because of the relaxation of the conservation condition on the component of momentum perpendicular to the surface. Hence, the half-width Γ of Eq. (4.3) can become large. This phenomenon broadens the spikes in the angular profile. However, we still expect much sharper features in the angular profiles for surface excitations than for bulk excitations. Also, $p_\perp(\vec{p}_\parallel^{\,0})$ will generally be a completely imaginary function which describes the decay of the excitation with distance from the surface. In such a case there would be no momentum-tuned sideband-diffraction resonances. To actually calculate the profiles for a surface excitation requires a model for $p_\perp = p_\perp(\vec{p}_\parallel^{\,0})$ and $\Gamma = \Gamma(\vec{p}_\parallel^{\,0})$. We defer such a calculation until Sec. V where we consider the excitation of surface plasmons in Al. In this system we can use jellium models for the plasmon spectral density.

V. SEMIQUANTITATIVE CALCULATIONS FOR PLASMON EMISSION IN Al

A. Model Description

In this section we present the results of semi-

quantitative calculations of the energy and angular profiles for inelastic diffraction from Al(100) for the case of plasmon emission. The appellation "semiquantitative" is used because for a nearly free-electron metal like Al it is anticipated that we may use semi-infinite jellium results for the plasmon-emission vertices.[17] We examine the case of the $\vec{g}=0$ (i.e., specular) beam for incident beam directions sufficiently close to normal incidence that angular-dependent renormalization effects on the vertices should not be important.[1] In the case of bulk plasmons we fit the theoretical form[15] of the plasmon damping parameter Γ to experimental high-energy-electron transmission measurements through Al films.[14] In the case of surface measurements we use the theoretical work of Feibelman[16] on Landau damping to obtain Γ.

Even for a weak-scattering material like Al, the Born approximation is inadequate for describing the elastic scattering. We expect, therefore, that multiple-scattering effects will be important in any realistic description of the inelastic scattering. We are thus forced to "renormalize" the elastic-scattering vertex in the two-step approximation[1] to take into account multiple scattering from the lattice. This renormalization procedure has been described elsewhere.[18, 23, 24] Therefore we merely summarize the relevant expressions. We continue to restrict our analysis to the case of s-wave scattering from an ion core in the solid.[18] In this limit we describe multiple intraplane scattering by replacing the single-site amplitude t in Eqs. (2.3) and (2.4) with a renormalized "subplane" amplitude determined by[18, 25]

$$\tau_\lambda(E)=t_\lambda(E)\,[1-t_\lambda\,G^{sp}(\vec{k},E)]^{-1}\,. \tag{5.1}$$

In Eq. (5.1) t_λ is the single-site scattering amplitude for an ion core in the λth plane (all sites in a given plane are assumed to be equivalent), and τ_λ is the total scattering amplitude for the λth plane. We refer the reader to Refs. 18 and 23–25 for a definition of the propagators G^{sp}. Completion of the renormalization procedure to include interplane as well as intraplane scattering requires the use of the complete layer amplitudes[18, 23–25] T_λ prior to the performance of the lattice-site sums whose result already is incorporated in Eq. (2.1).

As noted in the Introduction, we use the elastic-electron-scattering data to fix all of the parameters of both the renormalized elastic vertices and the electronic proper self-energy [i.e., see Eq. (2.9)]. In Fig. 12 we show a comparison between theory and experiment[26] for elastic electron diffraction from Al(100). The azimuthal angle ψ is defined with respect to the cube axes in the (100) face. The theoretical calculation makes use of the second-order perturbation-theory model of Ref. 18 which is adequate for a weak-scattering material like Al.[27] We regard Fig. 12 as a satisfactory comparison between theory and experiment in view of the simplicity of the theoretical model and the generally satisfactory description of the data over a wide range of incident angles. The relevant parameters obtained from Fig. 12 are $V_0=16.7$ eV, $\lambda_{ee}=8$ Å, $\delta_B=\frac{1}{5}\pi$, $\delta_s=\frac{1}{4}\pi$, where δ_B and δ_s are, respectively, the s-wave phase shifts for an ion core in the bulk or on the surface. Actually, this fit is almost indistinguishable from one using $\delta_s=\delta_B=\frac{1}{4}\pi$. Therefore in the interest of simplicity we use these latter phase shifts in calculating the inelastic diffraction profiles.

B. Bulk-Plasmon Emission

The effective loss vertex for coherent bulk-plasmon is[1, 17]

$$t_n(\vec{k}',\vec{k},\vec{p})=-i\,[(\pi e^2\hbar\omega_b/p^2)\,\Omega^2]^{1/2}\,\mathrm{sgn}(p_\perp)\,\theta(p_c-p)\,, \tag{5.2}$$

where Ω is the volume of a unit cell and p_c is the random-phase-approximation (RPA) cutoff wave vector for bulk plasmons[28] $p_c=1.2$ Å^{-1}. This leads to the following expression for the differential-scattering cross section[1]:

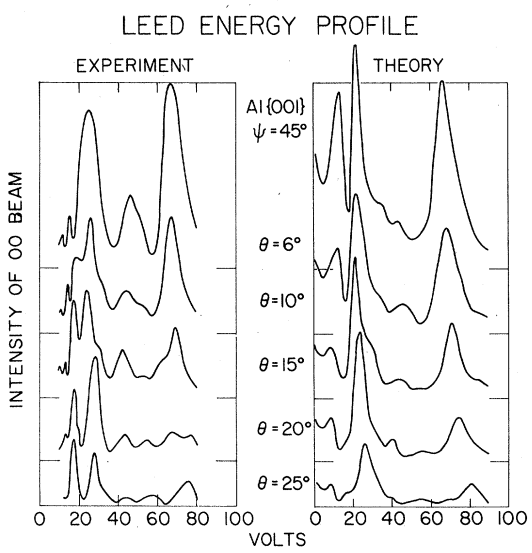

FIG. 12. Comparison of experimental (Ref. 26) and calculated elastic energy profiles for the (00) beam for Al(100). The calculations are based on the s wave inelastic collision model (Ref. 18) with the parameters given in the text and a lattice parameter of 4.042 Å. Calculated intensities are scaled for $\theta=6°$, 10°, 15°, 20°, 25° by 10, 6, 4, 3, 1.8, respectively. This scaling simulates the fact that, as noted in I, the damping and the inner potential (and the ion-core form factor) depend on the angle of incidence: effects which are not described by the model in the text. The azimuthal angle ψ is defined with respect to the simple-cubic (nonprimitive) unit cell of the fcc lattice.

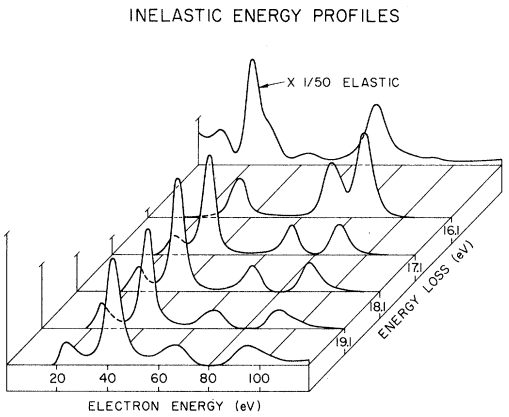

FIG. 13. Calculated elastic and inelastic energy profiles for the (00) beam from Al(100) for bulk-plasmon emission. Subplane elastic-scattering amplitudes (τ) have been employed to describe the elastic vertex. The profiles evaluated are for $\theta = \theta' = 15°$, $\psi = \psi' = 45°$, and the parameters used in calculating the profiles shown in Fig. 12. The scaling of the profiles is indicated by the bars on the left-hand side of the panel.

$$\left(\frac{d^2\sigma}{dE\,d\Omega}\right)_{bp} = \left(\frac{E-w}{E}\right)^{1/2}\left(\frac{2\pi m\hbar\omega_b}{h^2}\right)\left(\frac{m\pi e^2\Omega^2}{h^2 A}\right) \times \sum_{\vec{g}} \int_0^{p_c} \frac{dp_\perp}{2\pi} \frac{1}{(p_\parallel^2 + p_\perp^2)} \times \frac{2\Gamma(\vec{p}_\parallel^{\,0}, p_\perp)}{[w - \hbar\omega(\vec{p}_\parallel^{\,0}, p_\perp)]^2 + \Gamma^2(\vec{p}_\parallel^{\,0}, p_\perp)} \times M_{bp}(k_\perp(0,E), k_\perp'(0,E-w), p_\perp, \vec{g}) \times \left| A_b(\vec{g}, p_\perp, E, w) + A_c(\vec{g}, p_\perp, E, w)\right|^2 . \quad (5.3)$$

In writing Eq. (5.3) we have taken the zero-temperature limit because of the high energy of the plasmons relative to κT and have taken the plasmons to have a finite lifetime. However, if we consider plasmon damping, then from Eq. (2.7)

$$-2iN(-w)\,\mathrm{Im}D(\vec{p}, w) = 2\Gamma(\vec{p})/\{[w - \hbar\omega(\vec{p})]^2 + \Gamma^2(\vec{p})\} . \quad (5.4)$$

The damping parameter is given by[14, 15] $\Gamma(\vec{p}) = 1.06p^2$ eV and $\vec{p}_\parallel^{\,0}$ is given by Eq. (3.3a). With the presence of damping it is no longer possible to perform the $p_\perp$ integral analytically. A_b and A_c are given by Eqs. (2.3) and (2.4), respectively, with multiple-lattice-scattering effects being included as discussed previously. The plasmon dispersion relation is given by[13]

$$\hbar\omega(\vec{p}) = (16.0 + 3.37p^2)\,\mathrm{eV}. \quad (5.5)$$

In the expressions for both Γ and $\hbar\omega$ the momentum p is to be expressed in Å^{-1}. The envelope function M_{bp} is given by[1]

$$M_{bp}(k_\perp(0,E), k_\perp'(0,E-w), p_\perp, \vec{g}) = \left| [1 - R(k_\perp(0,E), k_\perp'(0,E-w), p_\perp, \vec{g})]^{-1} - [1 - R(k_\perp(0,E), k_\perp'(0,E-w), -p, \vec{g})]^{-1}\right|^2 . \quad (5.6)$$

Note that

$$\lim_{p_\perp \to 0} M_{bp} \propto p_\perp^2 \quad \text{as } p_\perp \to 0 . \quad (5.7)$$

Therefore the general features of the profiles for the $U = p_\perp$ coupling of Sec. III B 2 are expected to apply to this case.

In Fig. 13 we show calculated inelastic energy profiles for various loss energies. The profiles correspond to $\psi = \psi' = 45°$ and $\theta = \theta' = 15°$ with "planar" renormalization of the elastic vertex [i.e., in Eqs. (2.3) and (2.4) we have taken $t \to \tau$]. The elastic energy profile is shown in the panel to the rear of Fig. 13. The intensity of the inelastically diffracted beam is on the order of 1% of the intensity of the elastically diffracted beam. This should be well within the range of experimental observation. The elastic peak at about 70 eV is a suitable feature of the elastic profile that shows the doublet formation in the inelastic energy profile. The members of the inelastic doublet move further apart with increasing loss energy. There is no hint of the formation of the four-peaked sideband-diffraction structure in the energy profile. This is due to both multiple-scattering effects and plasmon damping. We only see one member of the inelastic doublet corresponding to the low-energy elastic peak at about 20 eV. This is because of the low-energy cutoff effect for non-normal beams as mentioned in Sec. III C. This cutoff occurs because the $\vec{p}_\parallel^{\,0}$ necessary to put the inelastic beam at $\theta' = 15°$ has such a large magnitude that the Lorentzian of Eq. (5.4) has no strength.

Inelastic angular profiles for bulk-plasmon emission are shown in Fig. 14 for a loss energy of 18 eV. Note the formation of the sideband-diffraction doublet structure as the incident beam energy moves over peak positions in the inelastic energy profile. For purposes of comparison, the inelastic energy profile is shown for $\theta' = 15°$ in the insert in the lower right-hand portion of the figure. The experimental observation of the change in the profile from a singlet to doublet and then back to a singlet with changing incident beam energy would constitute a verification of the sideband-diffraction phenomena.

Although we have taken into account some intralayer multiple-scattering effects at the elastic vertex, there are the further interlayer multiple-scattering renormalizations that can be made.[18, 23] It is worthwhile to consider how this additional multiple scattering might affect the inelastic angular profiles and in particular how it affects the features due to sideband diffraction. To check this we make a further renormalization. Prior to the layer sum leading to Eq. (2.1) we replace t with T^{SO} where

$$T_\lambda^{SO} = \tau_\lambda + \tau_\lambda \sum_{\lambda' \neq \lambda} G^{\lambda\lambda'} \tau_{\lambda'} \tag{5.8}$$

is the second-order perturbation-theory approximation[18] to T_λ. In performing the layer sum we only consider the case where both the λth and the λ'th planes are below the plane where the energy loss takes place. The results of this calculation for the angular profiles are shown in Fig. 15. In general the features of the profiles are qualitatively the same as in Fig. 14, although there is a quantitative change in some cases. We expect that the further multiple-scattering renormalization makes little additional change in the qualitative shape of the profiles[27] and hence the general features of sideband diffraction remain observable.

C. Surface-Plasmon Emission

The effective loss vertex for surface-plasmon emission is[1, 17]

$$t_n(\vec{k};\ \vec{k},\ \vec{p}) = (\pi e^2 \hbar \omega_s \Omega^2 / p_\parallel)^{1/2} \delta_{p_\perp, -ip_\parallel} \theta(p_m - p_\parallel) , \tag{5.9}$$

where Ω is the volume of a unit cell and p_m is a cutoff wave vector. This leads to the following expression for the differential-scattering cross section[1]:

$$\left(\frac{d^2\sigma}{dE d\Omega}\right)_{sp} = \left(\frac{E-w}{E}\right)^{1/2} \left(\frac{2\pi m \hbar \omega_s}{h^2}\right) \left(\frac{m\pi e^2 \Omega^2}{h^2 A}\right)$$

$$\times \sum_{\vec{g}} \frac{1}{p_\parallel^0} \frac{2\Gamma(p_\parallel^0)}{[w - \hbar\omega(p_\parallel^0)]^2 + \Gamma^2(p_\parallel^0)}$$

$$\times M_{sp}(k_\perp(0,E), k_\perp'(0, E-w), ip_\parallel^0, \vec{g})$$

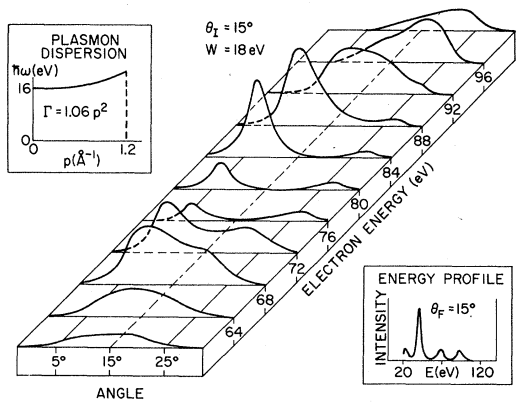

FIG. 14. Calculated inelastic angular profiles for the (00) beam from Al(100) for bulk-plasmon emission. The parameters used in the calculation are the same as for Fig. 13. The insert of the lower right shows an inelastic energy profile and the insert on the upper left illustrates the plasmon dispersion curve and the plasmon damping parameter.

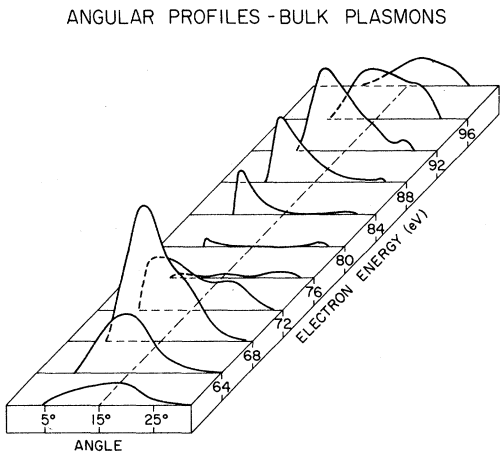

FIG. 15. Calculated inelastic angular profiles for the (00) beam from Al(100) for bulk-plasmon emission. The parameters used in the calculation are the same as for Fig. 14 except that the second-order scattering amplitude (T^{SO}) has been used instead of the layer amplitude (τ) as described below Eq. (5.8) in the text.

$$\times |A_b(\vec{g}, ip_\parallel^0, E, w) + A_c(\vec{g}, ip_\parallel^0, E, w)|^2 \theta(p_m - p_\parallel^0) . \tag{5.10}$$

In Eq. (5.10) the damping parameter is given by[16] $\Gamma(p_\parallel) = 1.28 p_\parallel$ eV; the dispersion relation is given by[13] $\hbar\omega(p_\parallel) = (11.1 + 5.2 p_\parallel)$ eV; with $p_\parallel$ being expressed in Å^{-1}. The envelope function M_{sp} is given by[1]

$$M_{sp}(k_\perp(0,E), k_\perp'(0, E-w), ip_\parallel^0)$$

$$= |1 - R(k_\perp(0,E), k_\perp'(0, E-w), ip_\parallel^0, \vec{g})|^{-2} , \tag{5.11}$$

where $p_\parallel^0 = |\vec{p}_\parallel^0|$ and $\vec{p}_\parallel^0$ is given by Eq. (3.3a). For the case of surface plasmons all integrals can be done analytically even in the presence of plasmon damping. Finally, we recall that whereas Eq. (5.9) recovers the well-known results of Stern and Ferrell[17, 29] for plane-wave electrons, in our cellular model the integration is in effect carried out only over the interior of the solid. Therefore Eqs. (5.10) and (5.11) do not correspond directly to the usual plane-wave results[17, 29] because we have used renormalized electron propagators inside the solid and have neglected the coupling of the surface plasmon to the bare electron outside the solid. This neglect changes the magnitude of the surface-plasmon emission process, but not its qualitative line shape. Both the size and detailed line shape of the inelastic cross section depend sensitively on the incident electron's wave function in the immediate vicinity of the diffuse electron cloud at the solid surface. As we do not know the wave function of the electron in this region, it seems to us most sensible at this stage in the development of the model to treat only the interaction inside the solid (in a fashion parallel to our analysis of bulk excita-

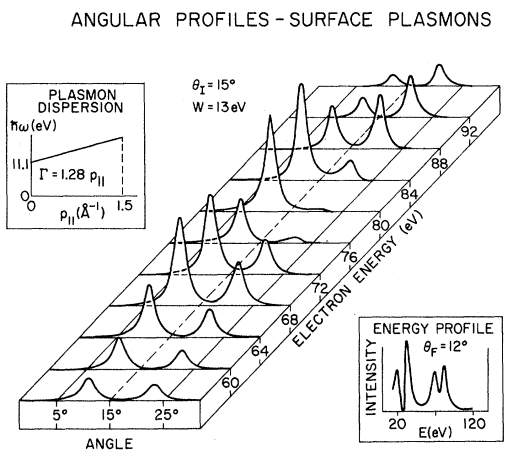

FIG. 16. Calculated inelastic angular profiles for the (00) beam from Al(100) for surface-plasmon emission. Layer elastic-scattering amplitudes (τ) have been used to describe the elastic vertex. The profiles are for $\theta = 15°$, $\psi = \psi' = 45°$, and the parameters of Fig. 12. The insert on the lower right shows an inelastic energy profile taken at $\theta' = 12°$. The insert on the upper left illustrates the plasmon dispersion curve and the plasmon damping parameter.

tions) and simply note that in detail (but not in qualitative outline) our predictions may differ from those of a more extensive calculation by factors of order unity.

In Fig. 16 we show calculated inelastic angular profiles for surface-plasmon emission for the case of electrons diffracting from Al(100). We have used the "planar" renormalization of the elastic vertex. In the presence of damping, the two spikes discussed in Sec. IV broaden into peaks having a finite width. Unlike the case of bulk-plasmon emission, the angular profiles always show a doublet structure. The positions of the doublet peaks are determined by the Lorentzian in Eq. (5.10). The envelope function M_{sp} exhibits no resonant behavior. The over-all size of each member of the doublet is determined largely by M_{sp} for a given E and w. The choice of cutoff momentum p_m has little effect on the profiles provided that it is large enough to include the peak positions. It merely indicates how far the low-intensity ends of the angular profile extend.

Because of the large qualitative difference in line shapes evident between Figs. 14 and 16, inelastic electron diffraction shows promise as a spectroscopic tool for identification of the type of excitation involved in the energy-loss procedure.

VI. SUMMARY AND CONCLUSIONS

In this paper we have investigated the predictions of the two-step diffraction model of inelastic diffraction.[1-3] We noted that an inelastic-diffraction experiment could be specified by the energy and angles of the incident beam, the angles of the diffracted beam and the amount of energy lost by the electrons during the scattering process. We defined intensity profiles where only one of these parameters was varied at a time and presented the results of numerical calculations for these profiles. We investigated the effect of different couplings between the beam electrons and electronic elementary excitations of the solid. We found that the inelastic energy profiles are rather insensitive to the particular form of the coupling used, but that the inelastic angular profiles can be quite sensitive to the nature of this coupling.

In general two peaks occur in the inelastic energy profile for each peak in the elastic energy profile. This is a general consequence of the two-step model of inelastic diffraction and the relevant conservation laws

$$E = w + E' , \tag{6.1}$$

$$\vec{k}_{\parallel} = \vec{k}'_{\parallel} + \vec{p}_{\parallel} - \vec{g} . \tag{6.2}$$

Under certain circumstances we found that for a bulk excitation these two peaks could split into four peaks due to the "accidental" conservation of the component of momentum perpendicular to the surface

$$\mathrm{Re}k_{\perp} = \mathrm{Re}[k'_{\perp} + p_{\perp} - G_{\perp}] , \tag{6.3}$$

where $G_{\perp}$ is a reciprocal-lattice vector for motion normal to the surface. We called this effect sideband diffraction. However, for realistic values of the excitation dispersion relation and the excitation lifetime, multiple-scattering effects would make its observation in the energy profiles highly unlikely.

Our examination of the inelastic angular profiles revealed that sideband diffraction produces a characteristic doublet structure for beam energies near peak positions in the inelastic energy profiles. We concluded that it should be possible to observe this effect experimentally, even in the presence of multiple-scattering effects, a realistic "flat" dispersion curve, and excitation lifetime effects.

We then considered surface excitations and noted that they do not produce a sideband-diffraction effect. We found that the inelastic angular profiles for surface plasmons should be quite different from those for bulk plasmons. Hence, at least in the case of plasmon excitation, it should be possible to use inelastic electron diffraction to determine the nature of the elementary excitation involved in the loss process.

Finally, we presented the results of semiquantitative calculations of the inelastic profiles for bulk- and surface-plasmon emission from Al(100). We could do this for Al because it is a nearly free-electron metal so we could use the sharp-junction

semi-infinite jellium model to obtain values for the electron-plasmon interaction,[17] the plasmon damping,[14–16] and the plasmon dispersion.[13] We used experimental elastic scattering data[26] to determine all adjustable electron-lattice and electron-electron interaction parameters in the calculation. We currently are undertaking more accurate calculations for Al using higher partial waves and taking into account the effects of lattice vibrations.[23,24] If we can predict accurately the inelastic scattering data for Al, we will turn to the transition metals and attempt to identify the various energy-loss mechanisms in these materials.

Note added in proof. Porteus and Faith[30] recently observed inelastic diffraction angular profiles from Al(111) and found remarkably good agreement with the predictions of our highly simplified model calculations. In particular they studied the angular profiles associated with an elastic Bragg peak at an energy of ~ 50 eV and found both the surface-plasmon doublet at a loss energy of 13 eV and what may be the sideband-diffraction structure associated with bulk plasmons at a loss energy of 15 eV. Evidently the theoretical free-electron dispersion relations[13] that we used in this paper have higher $p = 0$ values than those experimentally found. No structure was observed in the experimental profiles for a loss energy of 18 eV. Presumably this is due to the greatly reduced coupling strength as the loss energy increases (see Fig. 13). We are now engaged in analyzing their experimental data in an attempt to determine the actual surface plasmon dispersion relation for Al.

ACKNOWLEDGMENTS

The authors are indebted to Professor F. M. Propst for arousing their interest in this problem, to Professor Propst and Dr. J. O. Porteus for copies of their data prior to publication, to Dr. A. A. J. Howsmon for his assistance in parametrizing the elastic scattering from Al(100) and in constructing the inelastic scattering profiles, and to Mrs. V. Metze for invaluable assistance in programming.

---

*Work supported in part by the Advanced Research Projects Agency under Contract No. HC 15-67-C-0221 and in part by the Joint Services Electronics Program under Contract No. DAAB-07-67-C-0199.

†Present address: Sandia Laboratories, Albuquerque, N. M. 87115.

[1]C. B. Duke and G. E. Laramore, preceding paper, Phys. Rev. B, 3183 (1971).

[2]C. B. Duke, G. E. Laramore, and V. Metze, Solid State Commun. 8, 1189 (1970).

[3]C. B. Duke and G. E. Laramore, in Program of the Thirtieth Annual Conference on Physical Electronics, 1970 (unpublished), Paper C7; in *Proceedings of the Fourth LEED Seminar* (University of California, Irvine, Calif., 1970), p. 10.

[4]C. B. Duke, A. J. Howsmon, and G. E. Laramore, J. Vacuum Sci. Technol. 8, 10 (1971).

[5]C. B. Duke and C. W. Tucker, Jr., Phys. Rev. Letters 23, 1163 (1969); Surface Sci. 24, 31 (1971).

[6]J. A. Strozier, Jr. and R. O. Jones, Phys. Rev. Letters 25, 516 (1970).

[7]C. Davisson and L. H. Germer, Phys. Rev. 30, 705 (1927).

[8]J. C. Turnbull and H. E. Farnsworth, Phys. Rev. 54, 507 (1938).

[9]P. P. Reichertz and H. E. Farnsworth, Phys. Rev. 75, 1902 (1949).

[10]J. O. Porteus, in *The Structure and Chemistry of Solid Surfaces*, edited by G. A. Somorjai (Wiley, New York, 1969), p. 12-1.

[11]W. H. Weber and M. B. Webb, Phys. Rev. 177, 1103 (1969).

[12]M. P. Seah, Surface Sci. 17, 161 (1969).

[13]See for example, H. Raether, Ergeb. Exakt. Naturw. 38, 84 (1965).

[14]C. Von Festenberg, Phys. Letter 23, 293 (1966).

[15]D. F. DuBois and M. G. Kivelsons, Phys. Rev. 186, 409 (1969).

[16]P. J. Feibelman, Phys. Rev. 176, 551 (1968).

[17]J. I. Gersten, Phys. Rev. 188, 774 (1969).

[18]C. B. Duke, J. R. Anderson, and C. W. Tucker, Jr., Surface Sci. 19, 117 (1970).

[19]See for example, A. A. Abrikosov, L. P. Gor'kov, and I. Ee. Dzyaloshinskii, *Quantum Field Theoretical Methods in Statistical Physics* (Pergamon, New York, 1965), pp. 53–57.

[20]T. C. Cooper, J. M. Burkstrand, and F. M. Propst, Program of the Thirtieth Annual Conference on Physical Electronics, 1970 (unpublished) Paper C6; and (private communication).

[21]L. N. Tharp and E. J. Schreibner, J. Appl. Phys. 38, 3320 (1967).

[22]D. Edwards, Ph. D. thesis (University of Illinois, 1969) (unpublished).

[23]C. B. Duke and G. E. Laramore, Phys. Rev. B 2, 4765 (1970).

[24]G. E. Laramore and C. B. Duke, Phys. Rev. B 2, 4783 (1970).

[25]C. B. Duke and C. W. Tucker, Jr., Surface Sci. 15, 231 (1969).

[26]P. M. Marcus, D. W. Jepsen, and F. Jona, Surface Sci. 17, 442 (1969).

[27]C. W. Tucker, Jr. and C. B. Duke, *Proceedings of the Fourth LEED Theory Seminar* (University of California, Irvine, Calif., 1970), p. 18; Surface Sci. 24, 31 (1971).

[28]See, e.g., C. B. Duke, M. J. Rice, and F. Steinrisser, Phys. Rev. 181, 733 (1969).

[29]E. A. Stern and R. A. Ferrell, Phys. Rev. 120, 130 (1960).

[30]J. O. Porteus and W. N. Faith, Proceedings of the Fifth Low-Energy Electron Diffraction Seminar, 1971 (unpublished); and (private communication).